ELSEVIER

Contents lists available at ScienceDirect

Sustainable Energy Technologies and Assessments

journal homepage: www.elsevier.com/locate/seta





Computational study of natural ventilation in a sustainable building with complex geometry

Fei Xu^a, Songzhe Xu^{b,*}, Ulrike Passe^c, Baskar Ganapathysubramanian^d

- a Ansys Inc., USA
- ^b Scientific Computing and Imaging Institute, University of Utah, USA
- ^c College of Design, Iowa State University, USA
- d Department of Mechanical Engineering, Iowa State University, USA

ARTICLE INFO

Keywords: Natural ventilation Turbulence modeling Residual-based variational multiscale method Weak imposition of boundary conditions Complex building

ABSTRACT

We deploy a fully coupled thermo-fluidic finite element approach to simulating natural ventilation in a sustainably designed building with complex geometry. The 'interlock house' uses building design for climate control instead of mechanical means (such as air conditioning). Therefore, accurately modeling the natural ventilation flows is crucial to assess thermal comfort in such designs. A residual-based variational multiscale method (VMS) is employed, which is a Large Eddy Simulation (LES) type approach to turbulence modeling. The VMS formulation is further augmented with a weakly enforced boundary condition method to efficiently resolve the effect of boundary layers. We validate the framework using a canonical Rayleigh Bénard convection problem across different flow regimes. We deploy the framework to analyze thermal flows in the house under two natural ventilation configurations characterized by window opening strategies. Mesh convergence study using one of the configurations is performed to verify the framework. Comparisons of the flow fields and temperature distributions between the two scenarios are discussed. Air diffusion performance index (ADPI) and predicted mean vote (PMV) are computed to investigate thermal comfort in both configurations. This work illustrates the ability of the framework to comprehensively model and predict natural ventilation under various operating scenarios.

1. Introduction

According to the U.S. Energy Information Administration (EIA), buildings account for approximately 40% of the total U.S. energy consumption [1]. Thus, any incremental improvements in energy efficiency of buildings would play a significant role on the overall U.S. energy budget. Lower energy consumption also has many benefits to both human (health and economy) and environmental sustainability. Increasing interest has been drawn in understanding air ventilation and associated heat transfer in buildings in order to simultaneously increase the energy efficiency while maintaining indoor comfort. (Passive) natural ventilation is a promising alternative for energy-efficient ventilation in buildings [2–7] as wind and thermal energy are free resources. It also has the advantage to improve indoor air quality by exchanging indoor and outdoor air. As a result, taking account of the effects and subsequent benefits of natural ventilation will significantly contribute to designing sustainable buildings at reduced energy costs, and to this end, a good understanding of its physics is crucial for an optimal use of these freely available but uncontrollable resources, while providing adequate indoor thermal comfort.

As elaborated by Passe and Battaglia [8], the challenge for naturally ventilated building design is the direct interaction of spatial dimensions, program and use as well as opening design with respect to opening size. The flow path between the openings is as important as the understanding of boundary conditions. Therefore effective natural ventilation cannot be added after the design; it has to be integrated into design decisions from the start of a project. Hence, prediction of the dynamics of natural ventilation strategies to provide required air change rate and cooling capacity is critical. Yet reliable, easy to use computational design tools which can integrate all these aspects and provide feasible control strategies across all seasons have been lacking.

There has been increasing interest to model natural ventilation in buildings with a comprehensive review in Chen [9], who argues that computational fluid dynamics (CFD) is the most accurate and reliable modeling method. CFD is able to provide comprehensive flow and thermal information which is hard to predict by other methods. Since

E-mail address: songzhex@sci.utah.edu (S. Xu).

^{*} Corresponding author.

indoor natural ventilation usually presents combined natural and forced convection, it requires a detailed understanding of interactions between thermal buoyancy and pressure effect on the airflow, which is further complicated by frequent fluctuations in thermal and (inlet) flow boundary conditions due to uncontrollable wind loads. Accurate modeling of coupled momentum and heat transport of flows in complex, enclosed domains is possible via CFD, as shown by a variety of efforts [10–20], as well as in some other associated simulations for building energy efficiency, such as thermal optimization of windows [21–24].

Indoor natural ventilation usually exhibits mixed laminar and turbulent flow regimes during building operation with localized turbulence especially near the inlet. The simulation result near the inlet strongly affects the solution accuracy of interior fields, and therefore it needs to be accurately computed. The most widely used CFD turbulent modeling, Revnolds-averaged Navier-Stokes (RANS), usually requires site-specific and application-specific models [25], and has been proven not to work properly for natural ventilation [26-31]. This is likely due to the fact that RANS-based approaches need a priori information of flow regimes to identify laminar, transition and turbulent flows in different localized regions, which is usually not available ahead of time. This limitation of RANS-based models results in their failure to reliably predict the boundary heat transfer coefficient (Nusselt number), which is a fundamental parameter in investigating energy efficiency of buildings, across a wide range of flow conditions exhibited during building operation. In contrast, a more high-fidelity turbulent modeling based on Large Eddy Simulation (LES) is a promising alternative in accurately predicting thermal transport in enclosures. The LES model has been applied to natural convection in benchmark enclosure problems [32-35] with success, and later deployed in building simulations with accurate prediction of the effects of natural ventilation [36-38].

Motivated by the advantages of using LES in building simulations, we deploy a finite-element LES model based on the residual-based variational multiscale (VMS) method augmented with weakly enforced Dirichlet boundary condition method for buoyancy-driven flows [39] in this work. The VMS approach, originally proposed in [40-42], resembles LES by using variational projections in place of the traditional filtered equations in LES and focuses on modeling the fine-scale equations. Note that the VMS method does not employ any eddy viscosity or eddy conductivity, and has been shown to reliably perform accurate flow condition agnostic (mixed laminar and turbulent) simulations. In addition, the main reason that deters the building community to utilize LES-based approaches is because of the increased grid resolutions compared with RANS models, especially close to the boundaries to resolve the boundary layers. The higher simulation complexity and larger computational cost using LES-based approaches are comprehensively analyzed and compared with RANS-based models by Blocken [43]. Despite the increase in availability and ease of access of high-performance computing resources alleviating the computational burden of LES-based approaches, the reduction of overall computational efforts using these approaches is equally important to make them affordable and promising in building simulations. This is partially achieved by leveraging the weak imposition of Dirichlet boundary conditions, originally proposed in [44], which releases the point-wise no-slip flow condition and fixed thermal boundary condition at the Dirichlet boundaries and allows the flow velocity and temperature to vary on those boundaries by adding additional terms to ensure the accuracy of interior fluid fields. It results in substantial reduction in the mesh resolution required to resolve the steep gradients in flow and thermal boundary layers. The benefits of using weak imposition of boundary conditions for buoyancy-driven flows are detailed in [39]. The approach of VMS along with the weak imposition of boundary conditions has been successfully applied to many other engineering applications, and some recent works can be found in [45–50]. The main contribution of this work is to systematically deploy this approach to simulate a real-world, full-scale building with complex geometry and offer comprehensive insights into natural ventilation in this building. The case study building investigated here

has been monitored for multiple years with an extensive data acquisition system and validated for human thermal comfort using the adaptive comfort model as presented by ASHRAE [51,52].

The rest of the paper is outlined as follows. In Section 2, we lay out the formulations of VMS method and weak imposition of Dirichlet boundary conditions for natural ventilation. Section 3 illustrates two different configuration designs of natural ventilation in this building and mesh generation of the complex geometry. Section 4 performs mesh convergence study and presents numerical results of the simulated building. Section 5 draws conclusions and motivates future work of indoor ventilation simulations.

2. Variational multiscale and weak imposition of Dirichlet boundary condition formulations

In this section, we present all the numerical ingredients in our thermo-fluidic framework. The framework is comprehensively validated using a canonical Rayleigh–Bénard convection problem, which is a well investigated system for buoyancy driven flows. Details of the validation are provided in the Appendix.

2.1. Strong form of the continuous problem

The conservation laws of mass, momentum, and energy of incompressible flows may be written on a spatial domain $\Omega \subset \mathbb{R}^3$, with boundary Γ as

$$\frac{\partial \mathbf{u}}{\partial t} + \mathbf{u} \cdot \nabla \mathbf{u} = -\frac{1}{\rho} \nabla p + \nu \nabla^2 \mathbf{u} + \mathbf{f}$$
 (1)

$$\nabla \cdot \mathbf{u} = 0, \tag{2}$$

$$\frac{\partial T}{\partial t} + \mathbf{u} \cdot \nabla T = \alpha \nabla^2 T,\tag{3}$$

where \mathbf{u} is the velocity, ρ is the fluid density, p is the pressure, ν is the kinetic viscosity, T is the temperature, \mathbf{f} is the forcing function, and α is the thermal diffusivity. Under normal operating conditions, the Boussinesq approximation is a reasonable assumption. This approximates the thermal force in the momentum equation, \mathbf{f} , as a function of only T, and is modeled as $\mathbf{f}(T) = -\widehat{\mathbf{g}}\beta(T-T_r)\mathbf{e}_{\widehat{\mathbf{g}}}$, where $\widehat{\mathbf{g}}$ is the gravitational acceleration magnitude, $\mathbf{e}_{\widehat{\mathbf{g}}}$ is the unit vector pointing in the direction of gravity, β is the thermal expansion, and T_r is the reference temperature.

The Eqs. (1)–(3) are accompanied with specific boundary conditions, defined on $\Gamma = \Gamma^D \cup \Gamma^N$ with Dirichlet boundary $\Gamma^D = \Gamma^D_{\mathbf{u}} \cup \Gamma^D_T$ and Neumann boundary $\Gamma^N = \Gamma^N_{\mathbf{u}} \cup \Gamma^N_T$:

$$\mathbf{u} = \mathbf{u}_{g} \quad \text{on } \Gamma_{\mathbf{u}}^{\mathbf{D}}, \tag{4}$$

$$T = T_{\rm g}$$
 on $\Gamma_T^{\rm D}$, (5)

$$-\frac{p}{\rho}\mathbf{n} + \nu \nabla \mathbf{u} \cdot \mathbf{n} = \mathbf{h}_{\mathbf{u}} \quad \text{on } \Gamma_{\mathbf{u}}^{N}, \tag{6}$$

$$-\alpha \nabla T \cdot \mathbf{n} = \mathbf{h}_T \qquad \text{on } \Gamma_T^{N}, \tag{7}$$

where \mathbf{u}_g and T_g denote the prescribed velocity and temperature at the Dirichlet boundaries $\Gamma_{\mathbf{u}}^{\mathrm{D}}$ and Γ_{T}^{D} , respectively, $\mathbf{h}_{\mathbf{u}}$ and \mathbf{h}_{T} are the traction vector and heat flux at the Neumann boundaries $\Gamma_{\mathbf{u}}^{\mathrm{N}}$ and Γ_{T}^{N} , respectively, and \mathbf{n} is the unit outward wall-normal vector.

2.2. Semi-discrete variational multiscale formulations

We discretize the domain Ω into a collection of $N_{\rm cl}$ disjoint elements each denoted by Ω^e , such that $\Omega = \bigcup_{e=1}^{N_{\rm cl}} \Omega^e$. Let \mathscr{V}^h be the discrete space of trial solutions of velocity, pressure and temperature $\{\mathbf{u}^h, p^h, T^h\}$ sup-

ported on these elements. The superscript h denotes resolved coarse scales represented by the finite element discretization. The strong formulations (1)–(7) may be recast in a weak form and posed over this discrete space to produce the semi-discrete variational multiscale formulation for the natural ventilation problem: Find $\{\mathbf{u}^h,p^h,T^h\}\in\mathcal{V}^h$ such that $\forall\{\mathbf{w}^h,q^h,l^h\}\in\mathcal{V}^h$,

$$B^{\text{VMS}}(\{\mathbf{w}^h, q^h, l^h\}, \{\mathbf{u}^h, p^h, T^h\}) - F^{\text{VMS}}(\{\mathbf{w}^h, q^h, l^h\}) = 0,$$
(8)

where

$$\begin{split} & \mathcal{B}^{\text{VMS}} \left(\left\{ \mathbf{w}^{h}, q^{h}, l^{h} \right\}, \left\{ \mathbf{u}^{h}, p^{h}, T^{h} \right\} \right) \\ &= \int_{\Omega} \mathbf{w}^{h} \cdot \left(\frac{\partial \mathbf{u}^{h}}{\partial t} + \mathbf{u}^{h} \cdot \nabla \mathbf{u}^{h} \right) d\Omega + \int_{\Omega} \nabla \mathbf{w}^{h} : \nu \nabla \mathbf{u}^{h} d\Omega \\ &- \int_{\Omega} \frac{p^{h}}{\rho} \nabla \cdot \mathbf{w}^{h} d\Omega + \int_{\Omega} q^{h} \nabla \cdot \mathbf{u}^{h} d\Omega \\ &+ \int_{\Omega} l^{h} \left(\frac{\partial T^{h}}{\partial t} + \mathbf{u}^{h} \cdot \nabla T^{h} \right) d\Omega + \int_{\Omega} \nabla l^{h} \cdot \alpha \nabla T^{h} d\Omega \\ &- \sum_{e=1}^{N_{\text{cl}}} \int_{\Omega^{e}} \left(\mathbf{u}^{h} \cdot \nabla \mathbf{w}^{h} + \nabla q^{h} \right) \cdot \mathbf{u}' d\Omega - \sum_{e=1}^{N_{\text{cl}}} \int_{\Omega^{e}} \left(\mathbf{u}^{h} \cdot \nabla l^{h} \right) T' d\Omega - \sum_{e=1}^{N_{\text{cl}}} \int_{\Omega^{e}} \frac{p'}{\rho} \nabla \cdot \mathbf{w}^{h} d\Omega \\ &+ \sum_{e=1}^{N_{\text{cl}}} \int_{\Omega^{e}} \mathbf{w}^{h} \cdot \left(\mathbf{u}' \cdot \nabla \mathbf{u}^{h} \right) d\Omega - \sum_{e=1}^{N_{\text{cl}}} \int_{\Omega^{e}} \nabla \mathbf{w}^{h} : \left(\mathbf{u}' \otimes \mathbf{u}' \right) d\Omega \\ &+ \sum_{e=1}^{N_{\text{cl}}} \int_{\Omega^{e}} \nabla l^{h} \cdot \alpha_{\text{DC}} \nabla T^{h} d\Omega, \end{split}$$

and

$$F^{\text{VMS}}(\left\{\mathbf{w}^{h}, q^{h}, l^{h}\right\}) = \int_{\Omega} \mathbf{w}^{h} \cdot \mathbf{f}^{h} \, d\Omega + \int_{\Gamma_{\mathbf{u}}^{\mathbf{v}}} \mathbf{w}^{h} \cdot \mathbf{h}_{\mathbf{u}} \, d\Gamma + \int_{\Gamma_{\mathbf{u}}^{\mathbf{v}}} l^{h} \, \mathbf{h}_{T} \, d\Gamma.$$
 (10)

The fine-scale velocity, pressure, and temperature fields $\{\mathbf{u}',p',T'\}$ where the prime denotes the unresolved sub-scales of the discretization are modeled to be proportional to the coarse scale residuals of Eqs. (1)–(3), respectively, given by

$$\mathbf{u}' = -\tau_{M} \left(\frac{\partial \mathbf{u}^{h}}{\partial t} + \mathbf{u}^{h} \cdot \nabla \mathbf{u}^{h} + \frac{1}{\rho} \nabla p^{h} - \nu \nabla^{2} \mathbf{u}^{h} - \mathbf{f}^{h} \right), \tag{11}$$

$$p' = -\tau_{\rm C} \nabla \cdot \mathbf{u}^h, \tag{12}$$

$$T' = -\tau_{\rm E} \left(\frac{\partial T^h}{\partial t} + \mathbf{u}^h \cdot \nabla T^h - \alpha \nabla^2 T^h \right). \tag{13}$$

The fifth and sixth lines in Eq. (9) incorporate the additional terms added onto the standard Galerkin form and can be interpreted as the combination of classical stabilization terms such as streamline-upwind/Petrov–Galerkin (SUPG) and pressure-stabilizing/Petrov–Galerkin (PSPG) [53,54] and VMS turbulence modeling for the natural ventilation problem. Note that the VMS formulation of heat equation is simplified into a SUPG form. The stabilization parameters are defined as

$$\tau_{\mathrm{M}} = \left(\frac{4}{\Delta t^{2}} + \mathbf{u}^{h} \cdot \mathbf{G} \mathbf{u}^{h} + C_{M} \nu^{2} \mathbf{G} : \mathbf{G}\right)^{-1/2},\tag{14}$$

$$\tau_{\rm C} = (\tau_{\rm M} \text{tr} \mathbf{G})^{-1},\tag{15}$$

$$\tau_{\rm E} = \left(\frac{4}{\Delta t^2} + \mathbf{u}^h \cdot \mathbf{G} \mathbf{u}^h + C_E \alpha^2 \mathbf{G} : \mathbf{G}\right)^{-1/2},\tag{16}$$

where Δt is the time-step size, C_M and C_E are positive constants that can be derived from element-wise inverse estimates [55,56]. In current simulations, the values of C_M and C_E are both specified as 3. **G** is a mesh-dependent quantity calculated by the mapping from the isoparametric

element (ξ) to the physical element (x),

$$G_{ij} = \sum_{k=1}^{3} \frac{\partial \xi_k}{\partial x_i} \frac{\partial \xi_k}{\partial x_j},\tag{17}$$

and $\operatorname{tr} G$ is the trace of G. Finally, additional numerical stability is added to the Eq. (9) (in the last line) by introducing a discontinuity capturing term α_{DC} . This term stabilizes the energy equation where sharp temperature gradients or discontinuities are present, and is defined as

$$\alpha_{\rm DC} = C_{\rm DC} \frac{\left| \operatorname{Res}(T^h) \right|}{\max \left\{ \left| \nabla T^h \cdot \mathbf{G} \nabla T^h \right|^{\frac{1}{2}}, 10^{-15} \right\}},\tag{18}$$

where $C_{\rm DC}$ is a constant which is set to 0.5 in current simulations, and ${\rm Res}(T^h)$ is the coarse scale residual of Eq. (3).

2.3. Weakly imposed Dirichlet boundary conditions

Weak imposition of Dirichlet boundary conditions in the sense of Nitsche's method [57] is adopted into the natural ventilation problem. Decomposing the domain boundary Γ into $N_{\rm eb}$ surface elements each denoted by $\Gamma^{\rm b}$, the semi-discrete formulation becomes

$$\begin{split} &B^{\text{VMS}}\big(\big\{\mathbf{w}^{h},q^{h},l^{h}\big\},\big\{\mathbf{u}^{h},p^{h},T^{h}\big\}\big) - F^{\text{VMS}}\big(\big\{\mathbf{w}^{h},q^{h},l^{h}\big\}\big) - \sum_{b=1}^{N_{\text{ob}}} \int_{\Gamma^{b}\bigcap\Gamma^{D}_{\mathbf{u}}} \mathbf{w}^{h} \cdot \Big(\\ &-\frac{p^{h}}{\rho}\,\mathbf{n} + \nu \,\nabla \mathbf{u}^{h} \cdot \mathbf{n}\Big) \mathrm{d}\Gamma - \sum_{b=1}^{N_{\text{ob}}} \int_{\Gamma^{b}\bigcap\Gamma^{D}_{T}} l^{h} \alpha \nabla T^{h} \cdot \mathbf{n} \mathrm{d}\Gamma - \sum_{b=1}^{N_{\text{ob}}} \int_{\Gamma^{b}\bigcap\Gamma^{D}_{\mathbf{u}}} (\nu \,\nabla \mathbf{w}^{h} \cdot \mathbf{n} \\ &+ \frac{q^{h}}{\rho}\,\mathbf{n}\Big) \cdot \big(\mathbf{u}^{h} - \mathbf{u}_{g}\big) \mathrm{d}\Gamma - \sum_{b=1}^{N_{\text{ob}}} \int_{\Gamma^{b}\bigcap\Gamma^{D}_{\mathbf{u}}} \alpha \nabla l^{h} \cdot \mathbf{n} \big(T^{h} \\ &- T_{g}\big) \mathrm{d}\Gamma - \sum_{b=1}^{N_{\text{ob}}} \int_{\Gamma^{b}\bigcap\Gamma^{D}_{\mathbf{u}}} \mathbf{w}^{h} \cdot \big(\mathbf{u}^{h} \cdot \mathbf{n}\big) \big(\mathbf{u}^{h} - \mathbf{u}_{g}\big) \mathrm{d}\Gamma - \sum_{b=1}^{N_{\text{ob}}} \int_{\Gamma^{b}\bigcap\Gamma^{D}_{T}} l^{h} \big(\mathbf{u}^{h} \cdot \mathbf{n}\big) \big(T^{h} \\ &- T_{g}\big) \mathrm{d}\Gamma + \sum_{b=1}^{N_{\text{ob}}} \int_{\Gamma^{b}\bigcap\Gamma^{D}_{\mathbf{u}}} \tau^{B}_{M} \mathbf{w}^{h} \cdot \big(\mathbf{u}^{h} - \mathbf{u}_{g}\big) \mathrm{d}\Gamma + \sum_{b=1}^{N_{\text{ob}}} \int_{\Gamma^{b}\bigcap\Gamma^{D}_{T}} \tau^{B}_{E} l^{h} \big(T^{h} - T_{g}\big) \mathrm{d}\Gamma \\ &= 0, \end{split}$$

where $\Gamma^{D,-}_{\bf u}$ and $\Gamma^{D,-}_T$ represent velocity and temperature Dirichlet boundaries with ${\bf u}^h\cdot{\bf n}$ to be negative, respectively. The detailed interpretation of different terms in Eq. (19) can be found in [44,39]. The only parameters that need to be determined, τ^B_M and τ^B_E , are penalty-like stabilization parameters that help to satisfy Dirichlet boundary conditions and ensure the stability of the system. Following [44,39], we define $\tau^B_M = C^B_M \nu/h_B$ and $\tau^B_E = C^B_E \alpha/h_B$, where h_B is the wall-normal element size and C^B_M and C^B_E are positive constants that can be computed from an appropriate element-wise inverse estimates [56]. The values of C^B_M and C^B_E are both specified as 4 in current simulations.

3. Numerical implementation and problem design

3.1. Temporal discretization and solving strategies

To integrate the semi-discrete thermo-fluidic equations in time we employ the Generalized- α method, which was first introduced in [58] for structural dynamics and later extended to fluid dynamics in [59]. Generalized- α is an implicit, unconditionally stable, second-order method with control over high-frequency dissipation. The time step is chosen following CFL condition, and we make sure the CFL number is (roughly) less than 1 at each time step. We start to collect data after a quasi-steady state, and the time-averaged statistics of the solution are reported in Section 4. In addition, at each time step, the coupled nonlinear system is linearized using the Newton–Raphson method. At

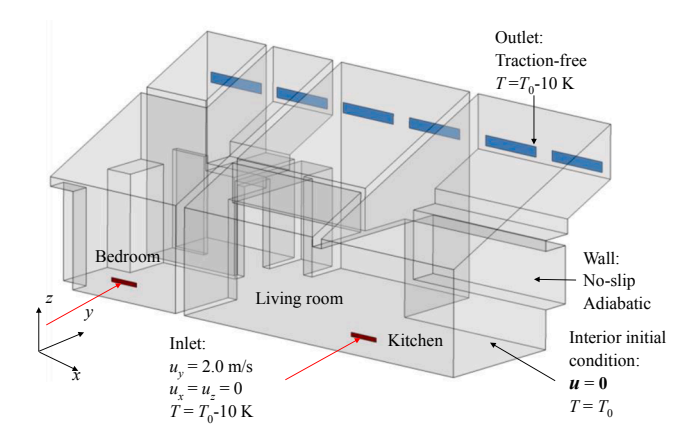


Fig. 1. Geometry of the building and problem setups. In configuration 1, only the window (inlet) on the right side is open, while for configuration 2, both windows are open.

each Newton–Raphson iteration, the linear system is solved iteratively using a Krylov subspace (KSP) type GMRES method [60,61] preconditioned with block Jacobi method. Note that we form the matrix directly from the complete VMS and weak imposition of boundary condition formulations without any special strategies to decouple the momentum and heat equations. Convergence criteria for both Newton–Raphson solver and GMRES solver are reasonably prescribed, and we ensure the solution is converged at each time step.

3.2. Building geometry and configuration design

The building with a modular design has a dimension of $11.82 \,\mathrm{m} \times 5.29 \,\mathrm{m} \times 4.72 \,\mathrm{m}$ in length (x axis), width (y axis), and height (z axis), respectively, as shown in Fig. 1. The origin of the coordinate system is placed at the bottom-left-front corner of the building. The building consists of three rooms that interlock together, i.e., (from right to left) kitchen, living room and bedroom. There are two windows located at the front wall (y=0) on left ($x=1.82 \,\mathrm{m}$) and right ($x=8.82 \,\mathrm{m}$) side, respectively, at a height of 0.46 m, through which wind at ambient low temperature of $T=293 \,\mathrm{K}$ comes into the building and cools the building at a initial high temperature at $T_0=303 \,\mathrm{K}$, and six clerestory windows located at back wall ($y=5.29 \,\mathrm{m}$) at a height of 3.69 m, through which indoor air exits the building. The front windows have the same dimension of 0.73 m \times 0.10 m, and the back windows have the same dimension of 1.47 m \times 0.24 m. In this work, we construct two scenarios of natural

ventilation in the building: Configuration 1 in which we only open the right front window as inlet, and Configuration 2 in which we open both front windows as inlet. In both configurations, we open all back windows as outlet. The boundary conditions are specified as follows. Velocity magnitude is prescribed to be uniform 2.0 m/s at inlets with direction normal to the inlet while traction-free condition is specified at the outlets. No-slip boundary condition is imposed at all walls. Temperatures at inlet and outlet are prescribed to be the same as ambient low temperature of 293 K. The building is assumed to be well insulated, and therefore adiabatic boundary condition is set at all walls.

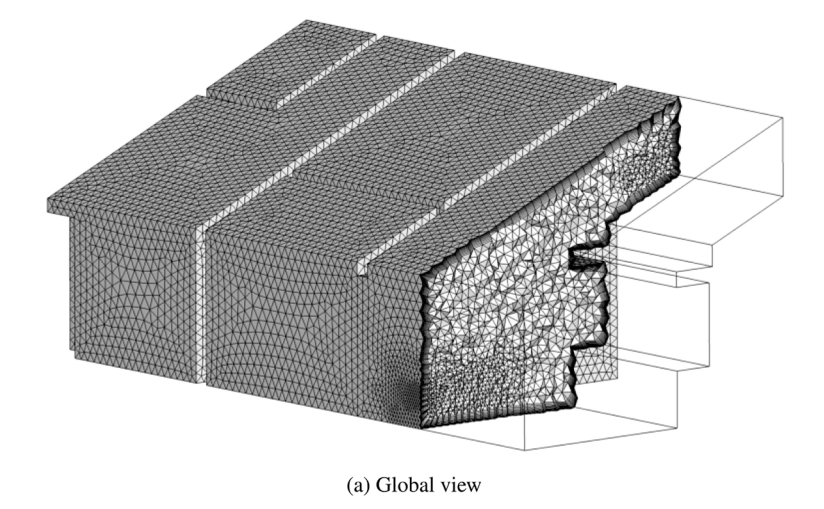
This problem setup results in a Reynolds number, $Re = 7.1 \times 10^5$, scaled by the length in the y direction (since air flows into the building through this direction) and the inlet velocity, a Grashof number, $Gr = 2.2 \times 10^{11}$, scaled by the temperature differential to be 10 K, and a Prandtl number, Pr = 0.71. These dimensionless parameters indicate a turbulent flow regime near the inlet window, and yield a Richardson number, which measures the importance of natural convection relative to forced convection, Ri = 0.45, resulting in a mixed convection flow regime.

3.3. Meshing strategy

To mesh the interior domain of the building, the following meshing strategy is used. We first discretize the building surfaces into triangles, with local refinements at windows as we speculate that most physics will take place around windows (especially around the inlet). From the triangulated surface mesh, we grow a total of 10 layers of thin prismatic elements to resolve the boundary layers. Finally, we fill the rest of the domain with pure tetrahedral elements to achieve the building mesh with mixed element types. To clearly visualize the mesh, we plot the meshes on a planar slice that cuts through the interior and a zoom-in slice to emphasize the boundary layer meshes as shown in Fig. 2. It can be seen that the window boundaries have the most refinement, and we also create inside refinement regions around the windows, to both better capture the fluid mechanics and heat transfer in these areas, and allow a smooth mesh size transition from the most refined window boundaries to the interior region with relatively large element size.

4. Results and discussion

In this section, we present a mesh independence study first to verify the framework by investigating the temperature and velocity magnitude profiles near the inlet using Configuration 1, i.e., only with right front window open as inlet. Then we present detailed comparisons of the



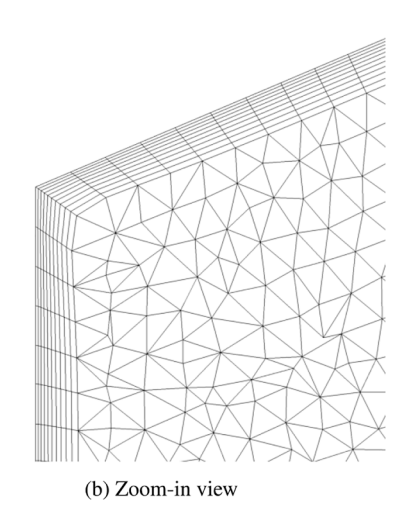


Fig. 2. Illustration of the finite element mesh in the fluid domain of the building: (a) a global view with a planar cut in *x* direction through the interior of the mesh; (b) a zoom-in slice to show the prismatic boundary layers and the tetrahedral elements in the interior.

Table 1
Statistics of the three meshes used for the mesh independence study using Configuration 1. Note the unit of the sizes is meter.

Mesh	First layer (prism) height	Inlet/outlet element size	Maximum surface element size	Number of elements
M1	0.01	0.08	0.16	985,507
M2	0.007	0.05	0.1	4,133,834
М3	0.005	0.03	0.06	15,958,302

temperature and velocity fields at different locations and flow field visualizations to investigate the natural ventilation in the two configurations. Finally, we present the air diffusion performance index (ADPI) and predicted mean vote (PMV) for thermal comfort analysis of these two configurations.

4.1. Mesh convergence study

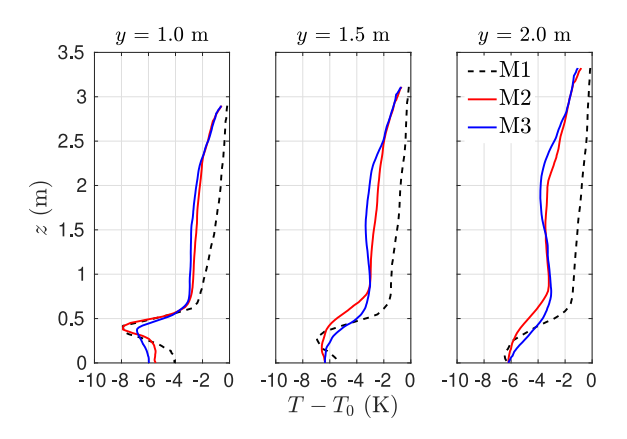
With the meshing strategy described in Section 3.3, we create three sets of meshes for a mesh independence study using Configuration 1. The mesh statistics for the three meshes, marked as M1, M2 and M3, respectively, are shown in Table 1. Same initial and boundary conditions are applied on the three meshes, and a time step size of 5.0×10^{-3} s is used in all of the simulations. We start to time-average the solution after a statistically quasi-steady state is reached. Afterwards, we plot the relative temperature and velocity magnitude profiles at x=9.2 m, in which plane the inlet is connected, with y=1 m, 1.5 m, and 2 m, to illustrate the mesh convergence results.

As shown in Fig. 3a, the temperature profile clearly converges as increasing mesh density. In addition, at $y=1.0\,\mathrm{m}$, where is the closest to the inlet window, the variation of temperature along z direction is much larger than the other two locations with a peak of low temperature at a height slightly lower than 0.5 m. This indicates the cold air is injected into the building creating a large temperature gradient near the inlet window, and as flowing deeper into the building, the incoming cold air is heated up by surrounding higher temperature air (transport of thermal energy) and demonstrates a much more smoothed temperature gradient along z direction. Similar behavior can be observed for air velocity magnitude as seen in Fig. 3b. The air velocity magnitude also convergences as increasing mesh density, and it has the largest gradient at a similar z location close to the inlet window. The velocity gradient is smoothed out and the velocity magnitude of the air current decays as it flows deeper inside, which indicates a loss of its kinetic energy and an exchange of its momentum with surrounding air. Note that in M2, the y⁺ parameter of the first layer element is around 40, which indicates that a satisfactory accuracy has been achieved on such a relatively coarse mesh. This clearly demonstrates the effect of weak imposition of boundary conditions in terms of reducing computational costs.

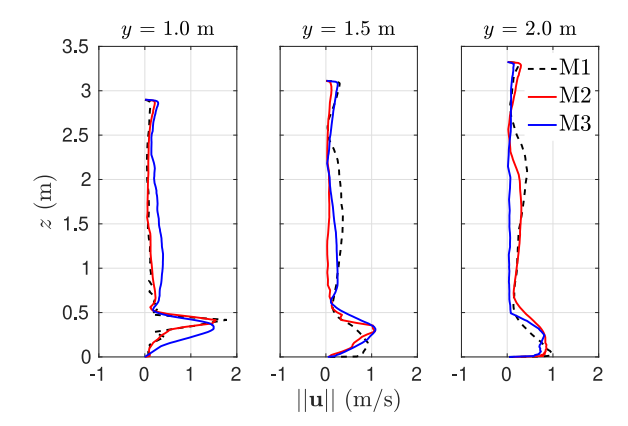
4.2. Comparisons between two configurations

We present temperature and velocity magnitude contours in the slices at x = 2.2 m, x = 6.0 m and x = 9.2 m, respectively, to visualize the airflow in the building. As discussed in the last section, the x = 9.2 m plane is in the kitchen, where the inflow is located (as well as in the Configuration 2). The x = 6.0 m plane represents a slice in the living room that is not directly connected with any cold air inlets in both configurations. The x = 2.2 m plane is in the bedroom, which is the farthest plane away from the inlet in Configuration 1 but also connected with an inlet in Configuration 2. These three slices across the x direction in areas with different flow patterns will give us a global insight of the natural ventilation inside the building. In addition, a slice at y = 1.5 m that intersects these three slices in the x plane is also presented for a more comprehensive visualization of both configurations as seen in Fig. 4. The velocity vectors in the slice at x = 9.2 m (which is connected to the right inlet) in both configurations are shown in Fig. 5 to visualize the air motion. Note that to highlight the velocity vectors, we replot the background velocity magnitude contours in a grey color table. We further present streamline visualizations in the overall building in both configurations. Finally, we overlap the two configurations and plot temperature and velocity magnitude profiles at each of above x coordinates with y = 1.0, 1.5 and 2.0 m, respectively, for more quantitative comparisons.

In Configuration 1, it can be observed from the velocity magnitude contours and vectors as shown in Fig. 4a and 5a that, cold air is injected through the inlet with a relatively high velocity, and it scatters and drops down due to the thermal buoyancy (can also be seen from temperature contours in Fig. 6a) resulting in a local turbulent flow region. Some air rises up and encounters falling airflow creating a major localized circulation zone in the kitchen as seen from Figs. 5a and 7a. Air velocity magnitude is very small in the other two slices in the x direction, as well as the slice in the y direction, which indicates a laminar flow regime in most regions of the building. This is a mixed case with both laminar and turbulent flows, and RANS models may fail to accurately predict the natural ventilation since it may cause excessive artificial turbulence when dealing with laminar flow regions. However, the residual-based VMS method automatically tunes the fine scale variables to approach to zero as the residuals of coarse scale are close to zero in laminar regions (coarse resolution is already able to capture physics in laminar regions), which enables it to perform accurate flow condition agnostic simulations (unlike RANS models) without any special treatments. In Configuration 2, the slices connected to inlets produce similar velocity magnitude contours as the Configuration 1 as shown in Fig. 4b, while the inflows present more fluctuations (also seen from temperature contours

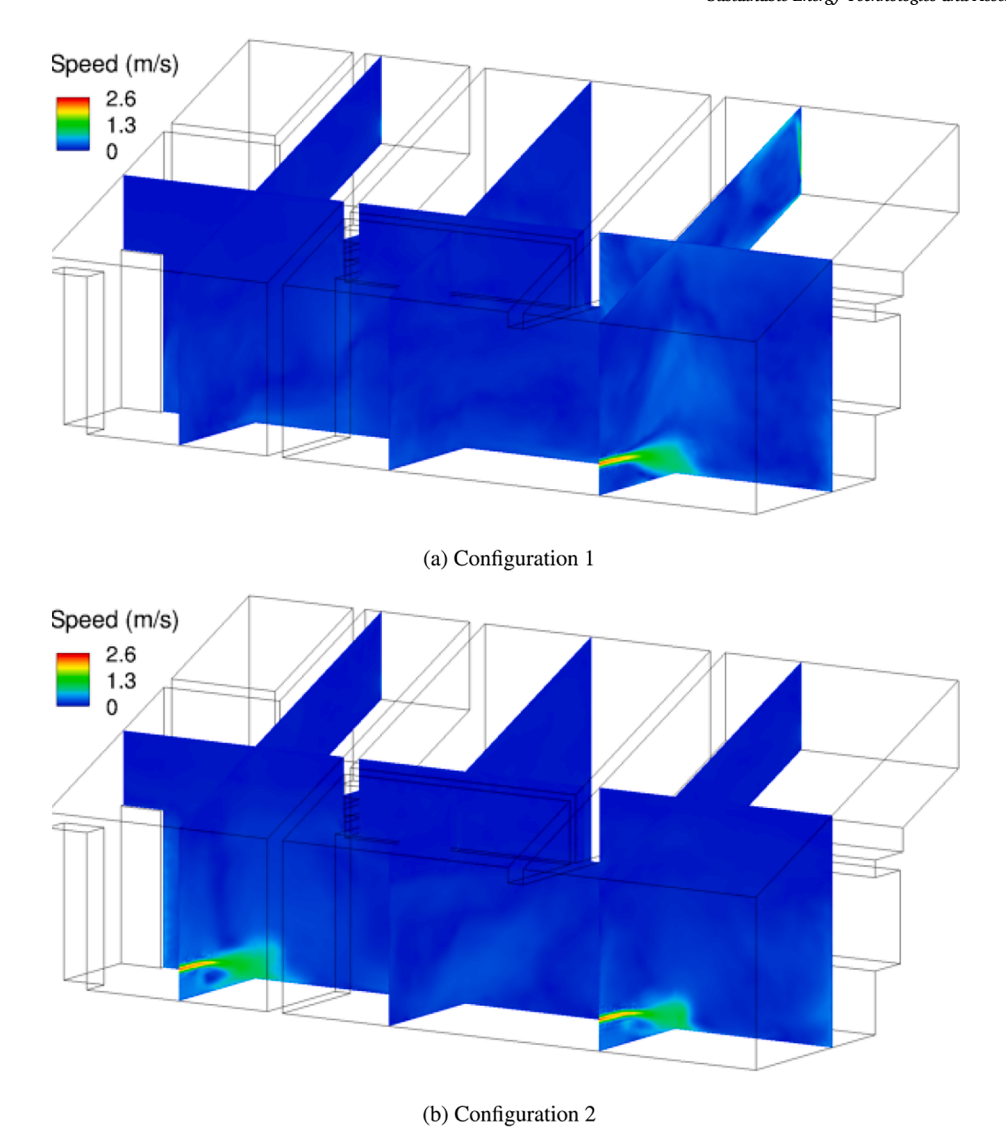


(a) Relative temperature $T - T_0$ plotted versus z-coordinates.



(b) Velocity magnitude ||u|| plotted versus z-coordinates.

Fig. 3. Results of mesh independence study at different y locations near the inlet (x = 9.2 m) using Configuration 1.



 $\textbf{Fig. 4.} \ \ \textbf{Visualization of velocity magnitude contours in the two configurations.}$

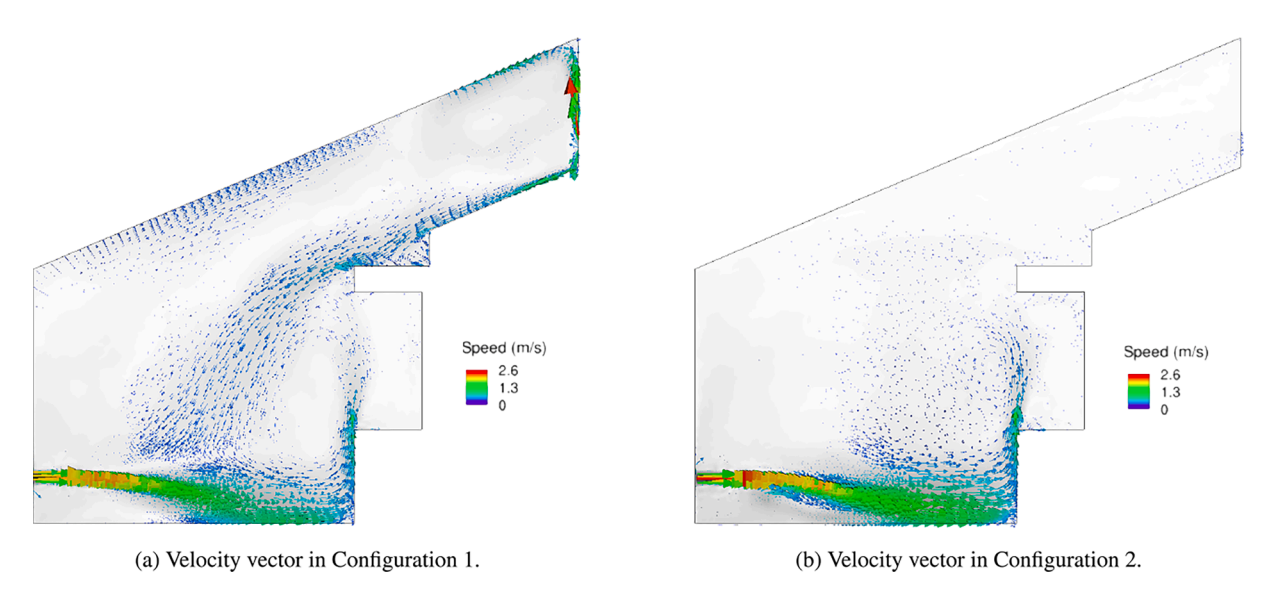


Fig. 5. Velocity vector visualization at an inlet (x = 9.2 m) in both configurations.

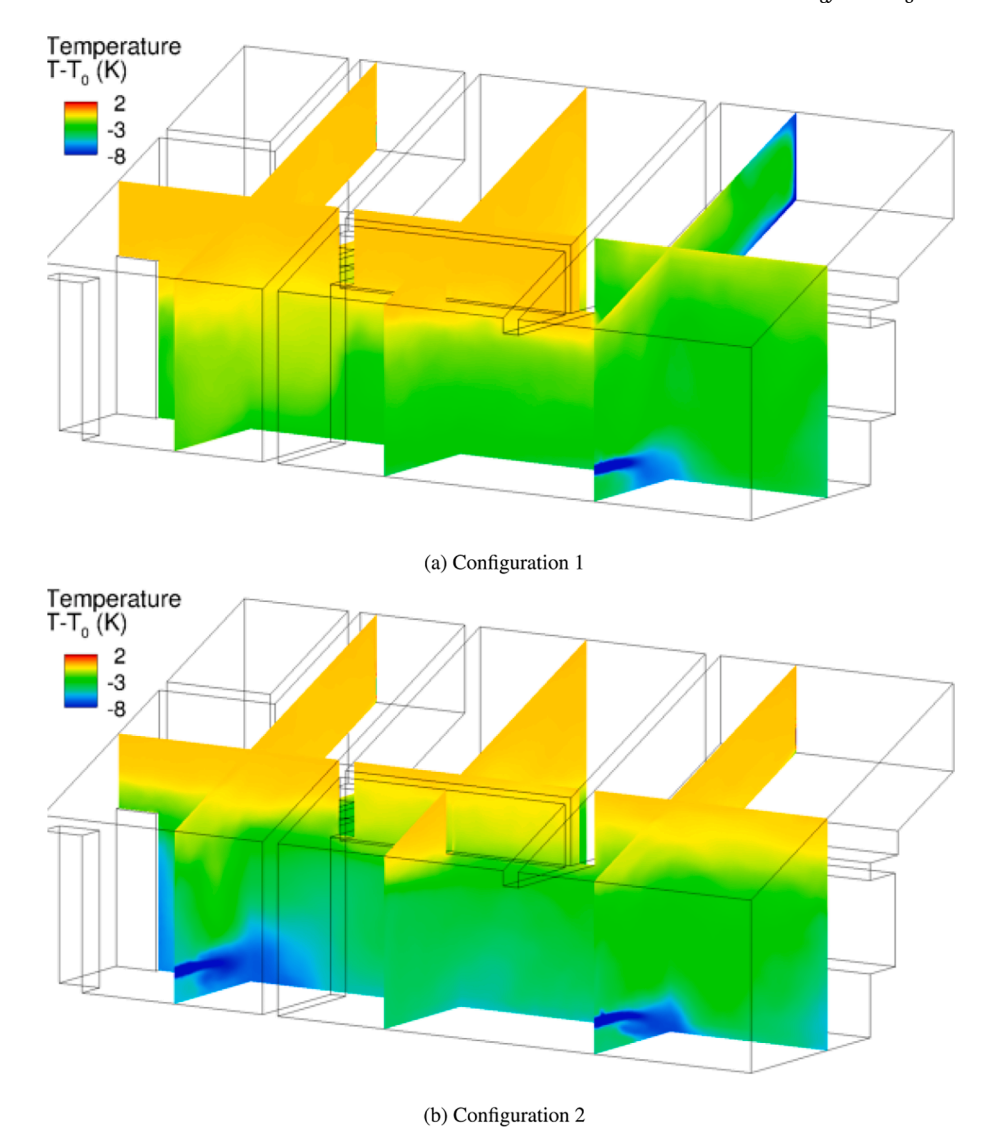


Fig. 6. Visualization of temperature contours in the two configurations.

in Fig. 6b), which we believe is due to the interaction between the two inlets in Configuration 2. A different circulation structure compared with the Configuration 1 in the kitchen can be observed from Fig. 5b. In the overall building, two individual air circulation zones (due to the barrier walls between bedroom and living room) can be seen from Fig. 7b.

In addition, for the temperature contours, it can be seen from Fig. 6a that Configuration 1 performs a localized cooling in the kitchen while most region in the bedroom (slice furthest away from the inlet) still remains relatively hot. The living room (middle slice) has a lower temperature at the bottom but higher temperature on the top. This indicates that the air flows mostly in the kitchen (can also be seen from Fig. 7a), and some cool air propagates to the living room mostly through the bottom (due to the barrier walls between living room and kitchen on the top) and gets further heated up in the living room. The energy (as well as momentum) transport into the bedroom is attenuated moving further away from the inlet. In contrast, as seen from Fig. 6b, Configuration 2 performs much better in cooling the global building, but still leaves the top of the building relatively hot (also due to the barrier walls on the top). This indicates a stronger transport and exchange of energy (as well as momentum) horizontally across the x direction due to the

communication of those two inlets in Configuration 2. Compared with Configuration 1, more horizontal air circulations are present between different rooms, as illustrated by Fig. 7b. It can also be observed that Configuration 2 cools the building uniformly in most regions resulting in a better thermal comfort of the space, as will become more quantitatively evident in the next section.

Finally, quantitative comparisons as shown in Fig. 8 match the qualitative analysis from visualizations. The comprehensive comparisons conclude that Configuration 1 performs better in cooling the kitchen, while Configuration 2 performs much better in cooling the overall building.

4.3. Thermal comfort analysis

We finally consider two indices of interest, Air diffusion performance index (ADPI) and predicted mean vote (PMV), for quantifying the thermal comfort of these configurations. The ADPI is a commonly used index that quantifies the performance of a ventilation system to generate spatial uniformity in air temperature and velocity and its contribution to thermal comfort. It is defined as the percentage of space where the criteria for effective draught temperature (EDT) and air velocity are

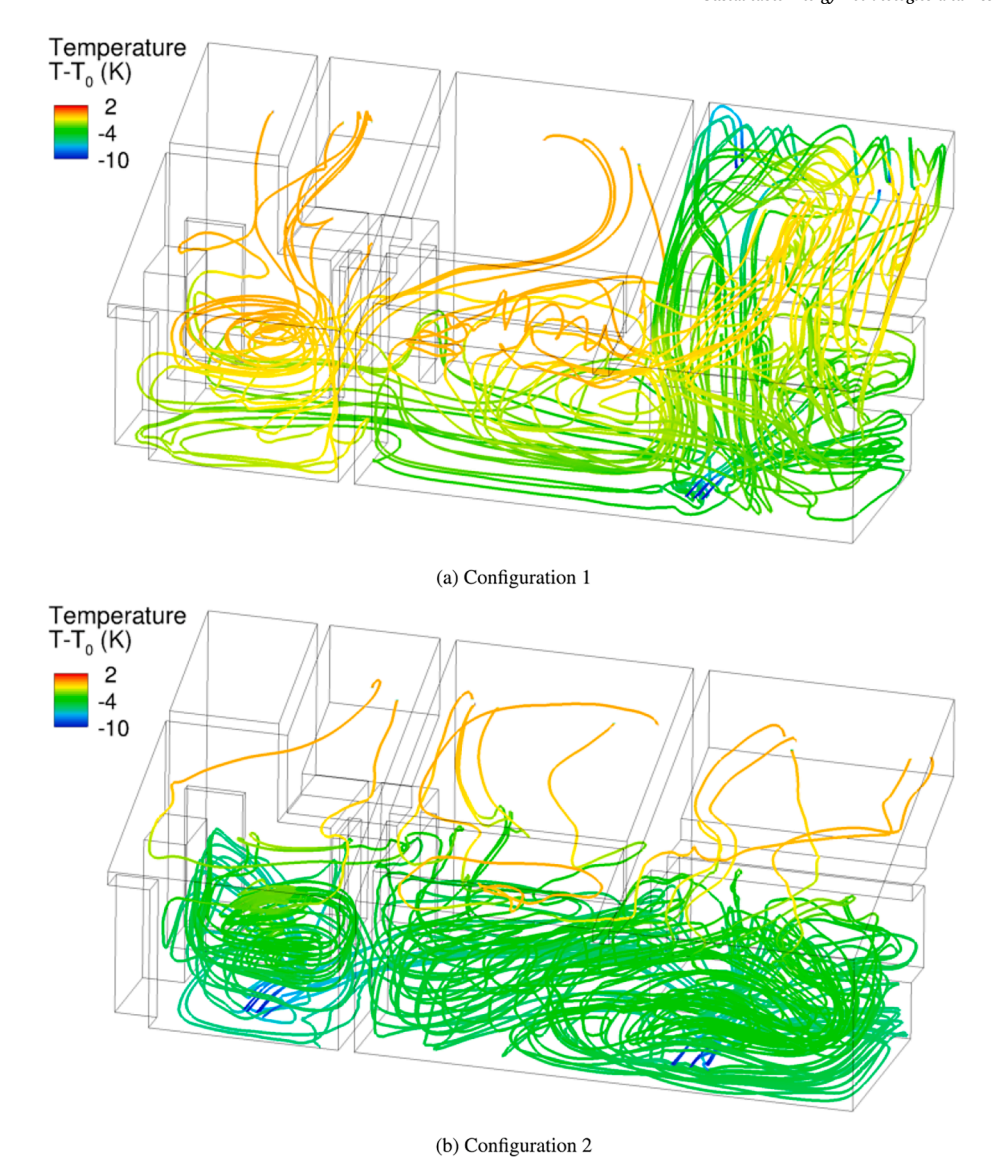


Fig. 7. Visualization of streamlines inside the building, colored by temperature $T - T_0$.

(21)

satisfied. The EDT is defined as

EDT =
$$(T - 273) - T_a - 8.0(\|\mathbf{u}\| - 0.15),$$
 (20)

where T_a is the average room dry-bulb temperature in ${^\circ \rm C}.$ ADPI is then defined as

$$\begin{split} ADPI = \frac{Space \ volume \ with (-1.7) \, ^{\circ}C \leqslant EDT \leqslant (+1.1) \, ^{\circ}C, \ and \|\textbf{u}\| \leqslant 0.35m/s}{Total \ space \ volume} \\ \times \ 100\%. \end{split}$$

It is generally agreed that a good ventilation system should be designed to achieve an ADPI higher than 80%, i.e., at least 80% of the total space meets the criteria [62].

In addition, the PMV developed by Fanger [63] is an index that measures human perception of comfort on a seven-point thermal sensation scale from -3 (cold) to +3 (hot). A zero value of PMV is ideal for thermal comfort, representing thermal neutrality. In buildings which incorporate a combination of natural ventilation and active heating and cooling, comfort zone is defined as a region with -0.5 < PMV < +0.5 [52]. Fanger's equation for PMV can be written as

$$PMV = (0.303 - \exp(-0.036M) + 0.028) \times \{(M - W) - 3.05 \times 10^{-3}(5733 - 6.99(M - W) - p_a) - 0.42((M - W) - 58.15) - 1.7 \times 10^{-5}M(5867 - p_a) - 0.0014M(34 - (T - 273)) - 3.96 \times 10^{-8}f_{cl}((t_{cl} + 273)^4 - T_m^4) - f_{cl}h_c(t_{cl} - (T - 273))\},$$
(22)

where M is the metabolic rate with a value of 80 w/m^2 , W is the mechanical power, which is assumed to be 0, T_m is the mean radiant temperature in K, which is assumed to be equal to T, P_a is the water vapor partial pressure in pascal, defined as

$$P_a = 611.21 \exp\left(\left(18.678 - \frac{T - 273}{234.5}\right) \left(\frac{T - 273}{257.14 + (T - 273)}\right)\right) h_u, \qquad (23)$$

 h_u is the humidity with a value of 60%, t_{cl} is the clothing surface temperature in $^{\circ}$ C, defined as

$$t_{cl} = 35.7 - 0.028(M - W) - I_{cl} \times \left\{ \left(3.96 \times 10^{-8} f_{el} \left(\left(t_{cl} + 273 \right)^4 - T_m^4 \right) + f_{cl} h_c (t_{cl} - (T - 273)) \right\},$$
(24)

 I_{cl} is the clothing insulation with a value of 0.11 m² k/w, h_c is the

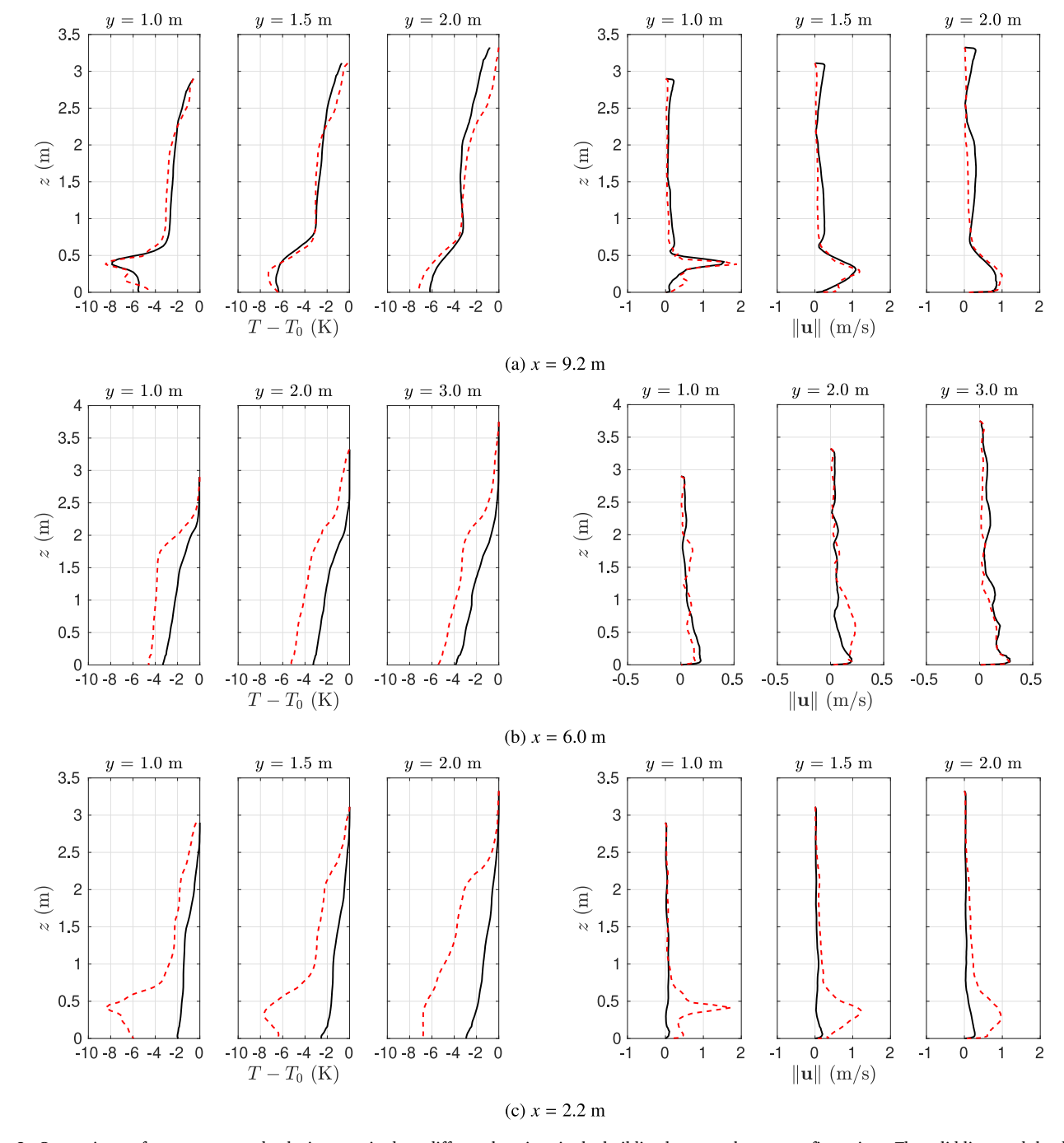


Fig. 8. Comparisons of temperature and velocity magnitude at different locations in the building between the two configurations. The solid lines and the dash lines denote the Configurations 1 and 2, respectively.

Table 2ADPI of the two configurations considering full volume vs. occupied space.

	Overall comfort zone	Occupied space (≤2 m) comfort zone
Configuration 1	44.33 %	67.60 %
Configuration 2	50.14 %	79.17 %

convective heat transfer coefficient in $w/(m^2k)$, defined as

$$h_c = \max(2.38 | t_{cl} - (T - 273) |^{0.25}, 12.1 \sqrt{||\mathbf{u}||}),$$
 (25)

 f_{cl} is the clothing surface area factor, defined as

$$f_{cl} = \begin{cases} 1.0 + 1.29I_{cl} & I_{cl} \leq 0.078 \text{m}^2 \text{k/w} \\ 1.05 + 0.645I_{cl} & I_{cl} > 0.078 \text{m}^2 \text{k/w}. \end{cases}$$
 (26)

Note that Eq. (24) is implicit for t_{cl} , and we use Newton method to iteratively solve for it.

The ADPI of the two configurations is presented in Table 2. It can be seen that when considering the full space, the two configurations both produce low ADPI values. This is usual for natural ventilation systems that exhibit large thermal gradients across the height. However, we are not concerned about the thermal comfort across the full height of the space, but rather consider the comfort in the occupied space. Therefore, we further compute ADPI for the occupied space defined as height less than 2 m, and it can be seen that the values of ADPI increase in the lower

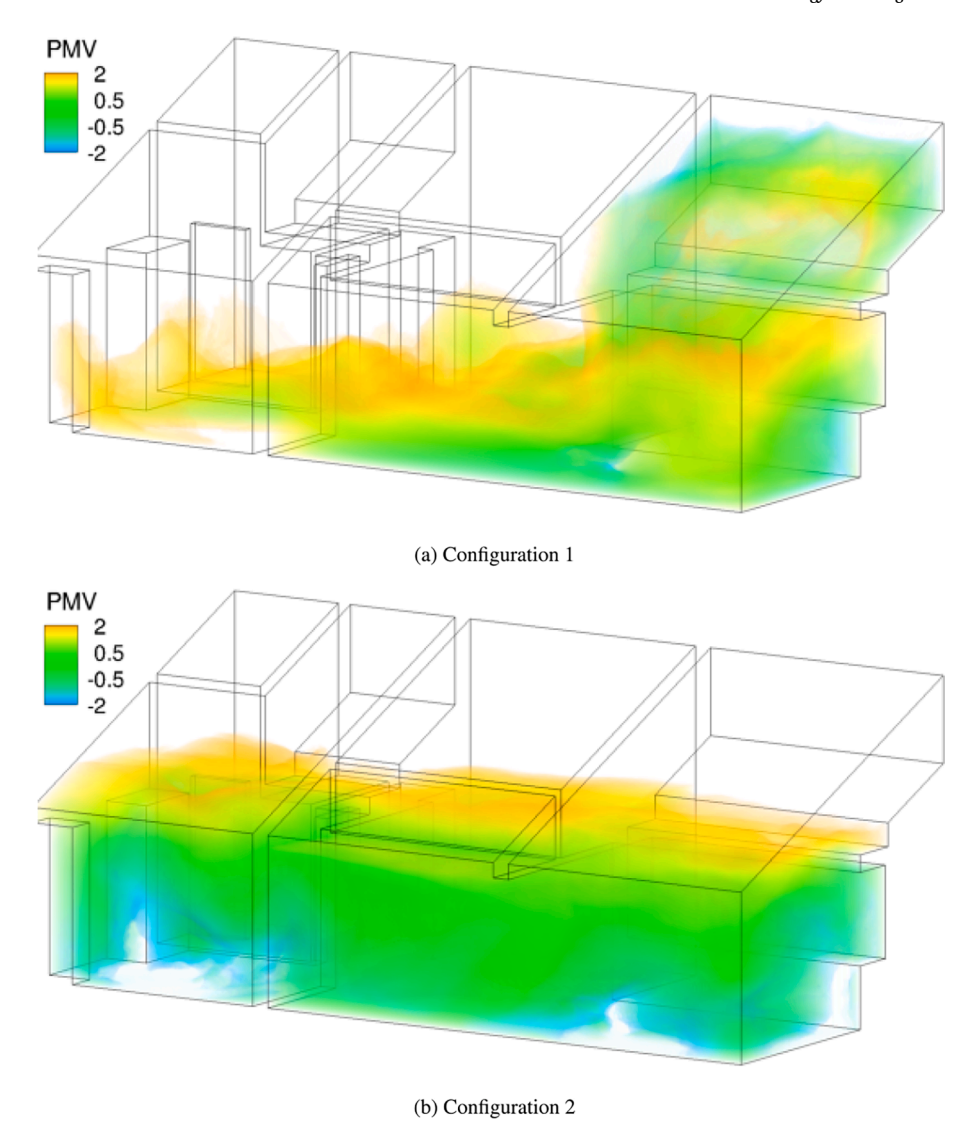


Fig. 9. Visualizations of PMV for thermal comfort. Only the spaces with PMV values between -2 and 2 are plotted.

spaces. The ADPI of Configuration 2 reaches almost 80% in this case, which suggests that Configuration 2 is a reasonable design of natural ventilation system for typical human residents. In addition, the PMV contours of the two configurations with values between -2 and 2 are shown in Fig. 9. It can be seen that the thermal comfort generally follows the cooling performance of each configuration as discussed in the last section (and seen from Figs. 6 and 7). Configuration 1 has a localized comfortable region in most space of the kitchen while Configuration 2 is able to obtain an overall thermal comfort uniformly across the lower space of the building (except near the two inlets). Again, the top of the building is not comfortable in both configurations (except some regions of the kitchen in Configuration 1), but it is not a concern for the aforementioned reasons.

5. Conclusions and future work

We deployed a residual-based variational multiscale framework augmented with weakly imposed Dirichlet boundary condition method to simulating natural ventilation under two configurations of cooling a complex building. This approach automatically enables accurate flow condition agnostic simulations (unlike RANS models) with reduced computational efforts in boundary layers. This framework is validated using a canonical Rayleigh-Bénard convection problem. A mesh convergence study for temperature and velocity magnitude profiles near the inlet window using Configuration 1 is performed to verify this framework in simulating the complex building. Visualizations of temperature and velocity magnitude contours as well as velocity vectors and streamlines are presented to offer comprehensive insights of the natural ventilation in these two configurations. Comparisons between them show that Configuration 2 performs much better in cooling the global building, while Configuration 1 localizes the cooling and performs better in the kitchen. ADPI is computed for the occupied volume for these two configurations, and suggests that Configuration 2 is a good design for ensuring thermal comfort. PMV is also computed for thermal comfort of both configurations. It shows the thermal comfort generally matches the cooling performance in both configurations, and Configuration 2 is able to create an overall thermal comfort uniformly across the lower space of the building.

The results in this paper have demonstrated the robustness and accuracy of our framework in simulating natural ventilation across a wide range of flow regimes in a very complex geometry. The parameter-free nature of the framework makes it seamless to be used in variations of natural ventilation designs. Some design-optimization management tools can also be easily integrated with the framework to efficiently evaluate and improve the performance of specific natural ventilation designs. We also plan to deploy this framework to further investigate natural ventilation in more realistic scenarios – for example, with human and furniture inside the building subject to more complex and realistic flow and thermal boundary conditions.

CRediT authorship contribution statement

Fei Xu: Methodology, Software, Validation, Formal analysis, Investigation, Data curation, Writing - original draft, Writing - review & editing, Visualization. **Songzhe Xu:** Conceptualization, Methodology, Formal analysis, Resources, Writing - original draft, Writing - review &

editing, Visualization, Supervision. **Ulrike Passe:** Conceptualization, Writing - review & editing, Project administration, Funding acquisition. **Baskar Ganapathysubramanian:** Conceptualization, Writing - review & editing, Project administration, Funding acquisition.

Declaration of Competing Interest

The authors declare that they have no known competing financial interests or personal relationships that could have appeared to influence the work reported in this paper.

Acknowledgement

The authors acknowledge supercomputing resources in the Center for High Performance Computing (CHPC) at the University of Utah. Baskar Ganapathysubramanian and Ulrike Passe acknowledge partial support from NSF 1855902. The authors thank Aditya Kommajosula for the help with mesh generation.

Appendix. Validation of the framework using a Rayleigh-Bénard convection problem

In this section, we carry out a validation of our framework using a canonical problem of buoyancy driven convection – Rayleigh–Bénard convection problem. We consider the standard, non-dimensional case of an enclosed box with temperature difference across the vertical walls. We validate our framework in a laminar case ($Ra = 1.89 \times 10^5$) and a turbulent case ($Ra = 1.5 \times 10^9$), respectively, to illustrate the accuracy of the framework in simulating different flow regimes without special treatments. No-slip velocity boundary conditions are prescribed on all walls in both cases. High temperature is set on the left (x = 0) wall while low temperature is set on the right (x = 1) wall. Note that in the laminar case, we impose adiabatic boundary condition on other walls while in the turbulent case, we impose experimentally measured temperatures in [32] on horizontal walls. Gravity is along the z direction. The geometry and the boundary condition setup for the Rayleigh–Bénard problem are illustrated in Fig. 10.

The laminar case employs a unit cubic domain with a mesh of 722,257 tetrahedral elements, while the turbulent case employs a cuboid domain of a size of $1 \times 0.32 \times 1$ with a mesh of 837,833 tetrahedral and 1,213,824 prism elements. The simulation of the laminar case is carried out until a steady state is reached, while the time-averaged solution is obtained for the turbulent case after a fully developed flow field is achieved. We first compute the average Nusselt number, \overline{Nu} , over the hot wall for the laminar case and along the vertical median line on the hot wall for the turbulent case, and compare \overline{Nu} with other numerical and experimental results in references [64,65] for the laminar case and [32] for the turbulent case, as shown in Table 3, respectively. In both cases, \overline{Nu} 's from our simulated results match the data in the references very well.

To further illustrate the good prediction of the physics inside the entire fluid domain, we then plot mean temperature and velocity profiles along horizontal and vertical median lines, and compare with references. Results from the laminar and the turbulent cases are shown in Figs. 11 and 12, respectively, which demonstrate overall excellent agreement between our simulations and the reference results. Note that in the experiments, it is challenging to maintain a perfectly adiabatic thermal boundary condition. As a result, in the laminar case, it is evident that the experimental results [66] do not present a zero heat flux at horizontal boundaries. In the turbulent case, as we impose the experimentally measured temperatures on horizontal walls, a closer agreement with experimental results can be observed at the horizontal boundaries, while visible discrepancy can still be observed. This could again be due to the difficulty in maintaining constant temperatures at such a large Ra number in the experiment. Nevertheless, for the temperature along vertical median line, in the laminar case, our result matches the other numerical results very well, and in the turbulent case, our result better matches the experimental result than the plotted numerical references. These comparisons comprehensively validate this thermo-fluidic framework for accurately predicting buoyancy driven convection in enclosures, and illustrate the capability of this framework to simulate natural ventilation in complex buildings.

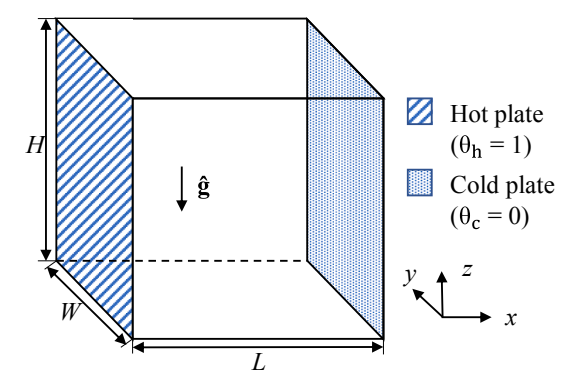


Fig. 10. Schematic of the Rayleigh-Bénard convection problem.

Comparison of \overline{Nu} for the two Rayleigh–Bénard problems with experimental and numerical reference values.

Ra	This work	References
1.89×10^5	5.39	5.25 [64], 5.31 [65]
1.5×10^9	58.08	54.0 (Exp), 58.0 (LES), 57.5 (DNS) [32]

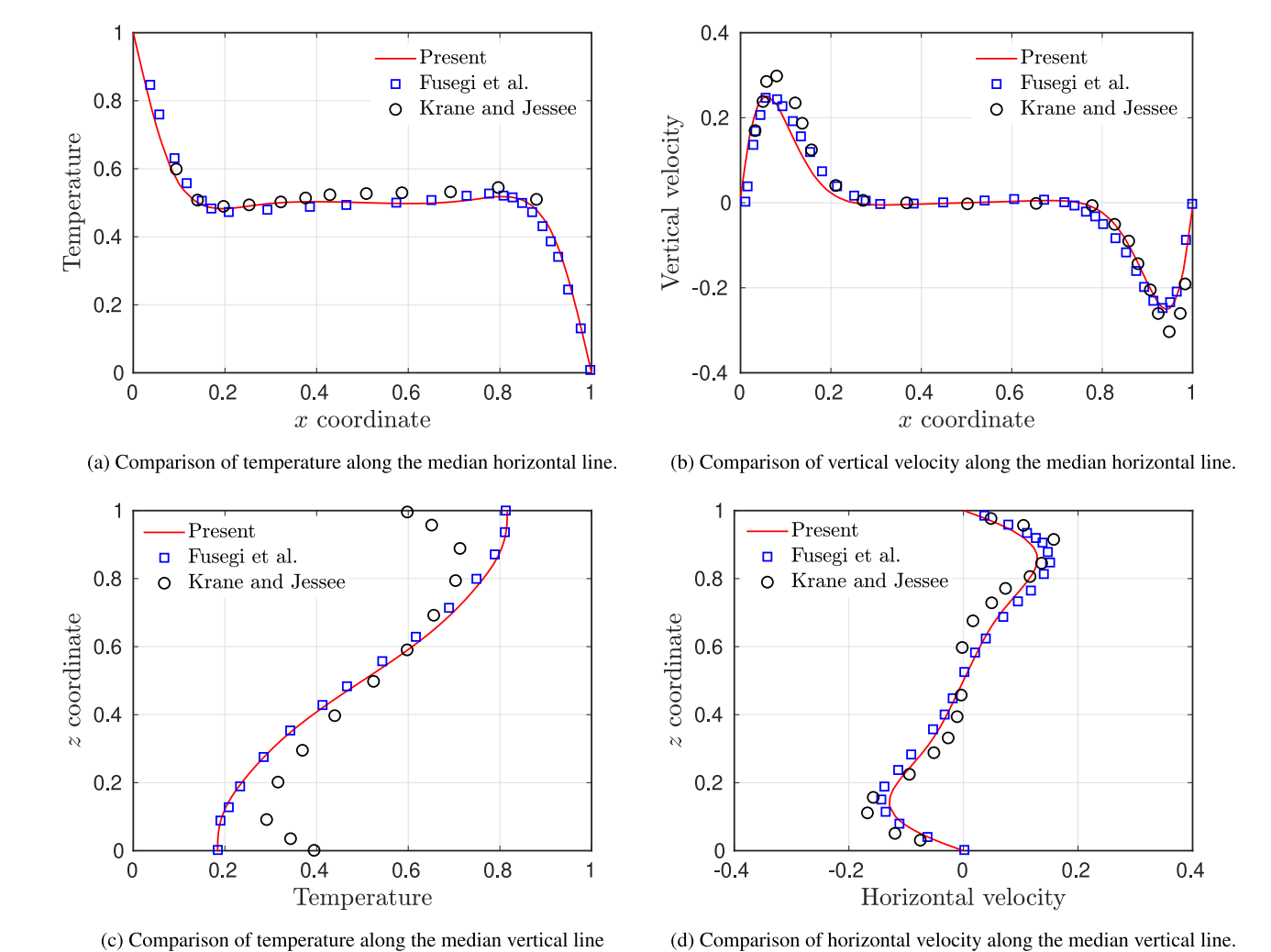
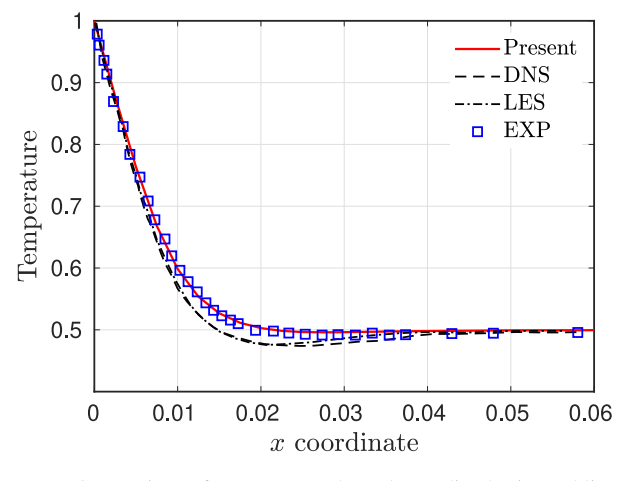
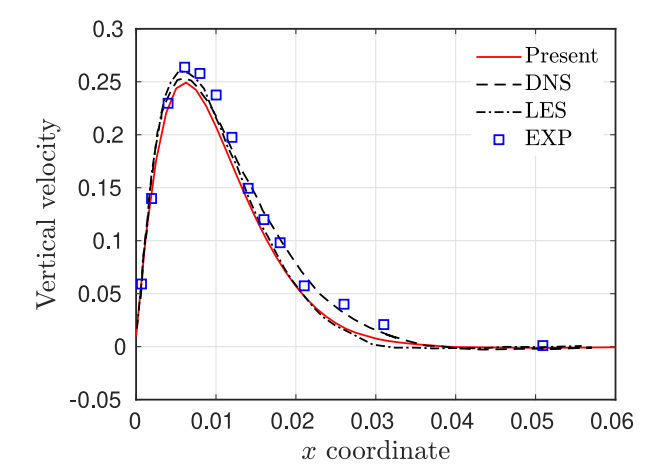


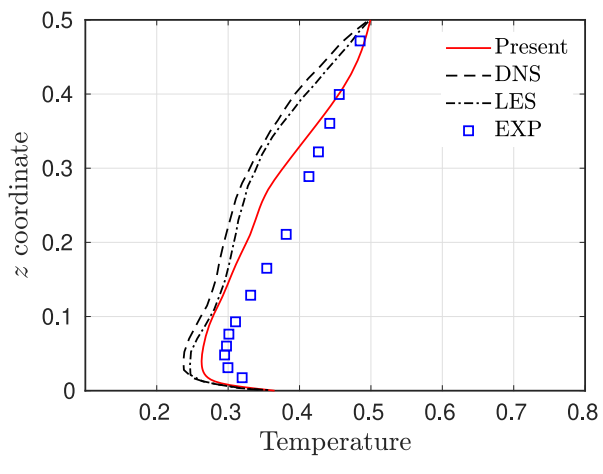
Fig. 11. Validation of a laminar case with $Ra = 1.89 \times 10^5$ using a Rayleigh–Bénard convection problem. Results from Fusegi et al. [64] and Krane and Jessee [66] are plotted as references.

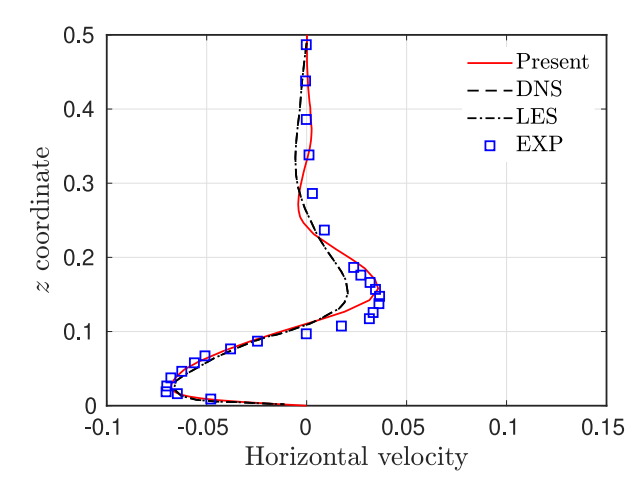




(a) Comparison of temperature along the median horizontal line.







- (c) Comparison of temperature along the median vertical line.
- (d) Comparison of horizontal velocity along the median vertical line.

Fig. 12. Validation of a turbulent case with $Ra = 1.5 \times 10^9$ using a Rayleigh–Bénard convection problem. Numerical and experimental results from Salat et al. [32] are plotted as references.

References

- [1] Office of Energy Efficiency & Renewable Energy (EERE). Buildings Energy Data Book. https://openei.org/doe-opendata/dataset/buildings-energy-data-book, 2011. US Department of Energy, Washington, D.C.
- [2] Oldewurtel F, Parisio A, Jones CN, Gyalistras D, Gwerder M, Stauch V, Lehmann B, Morari M. Use of model predictive control and weather forecasts for energy efficient building climate control. Energy Build 2012;45:15–27.
- [3] Petersen S, Svendsen S. Method for simulating predictive control of building systems operation in the early stages of building design. Appl Energy 2011;88(12): 4597–606.
- [4] Privara S, Cigler J, Váňa Z, Oldewurtel F, Sagerschnig C, Žáčeková E. Building modeling as a crucial part for building predictive control. Energy Build 2013;56: 8–22.
- [5] Privara S, Širokỳ J, Ferkl L, Cigler J. Model predictive control of a building heating system: the first experience. Energy Build 2011;43(2):564–72.
- [6] Rao CV, Rawlings JB. Linear programming and model predictive control. J Process Control 2000:10(2):283–9.
- [7] Salsbury T, Mhaskar P, Qin SJ. Predictive control methods to improve energy efficiency and reduce demand in buildings. Comput Chem Eng 2013;51:77–85.
- [8] Passe U, Battaglia F. Designing spaces for natural ventilation: an architect's guide. Routledge; 2015.
- [9] Chen Q. Ventilation performance prediction for buildings: a method overview and recent applications. Build Environ 2009;44(4):848–58.
- [10] Fontanini A, Olsen MG, Ganapathysubramanian B. Thermal comparison between ceiling diffusers and fabric ductwork diffusers for green buildings. Energy Build 2011;43(11):2973–87.
- [11] Fontanini A, Vaidya U, Ganapathysubramanian B. A methodology for optimal placement of sensors in enclosed environments: a dynamical systems approach. Build Environ 2016;100:145–61.

- [12] Deza M, Ganapathysubramanian B, He S, Passe U. High fidelity CFD modeling of natural ventilation in a solar house. ASME 2015 international mechanical engineering congress and exposition 2015.
- [13] Passe U, Ganapathysubramanian B, He S, Vansice K, Xu S. An integrated experimental-computational investigation of connected spaces as natural ventilation typologies. In: 2016 Proceedings of the symposium on simulation for architecture and urban design: 2016.
- [14] Passe U, Ganapathysubramanian B, Yesilata B. The harran houses as a case study for solar assisted passive ventilation and cooling. In: Proceedings of the Turkish solar energy conference SolarTR; 2014.
- [15] Chen Q. Comparison of different k- ε models for indoor air flow computations. Numer Heat Transfer B Fundam 1995;28(3):353–69.
- [16] Chen Q, Xu W. A zero-equation turbulence model for indoor airflow simulation. Energy Build 1998;28(2):137–44.
- [17] Chen Q. Prediction of room air motion by reynolds-stress models. Build Environ 1996;31(3):233–44.
- [18] Zhai ZJ, Chen QY. Performance of coupled building energy and cfd simulations. Energy Build 2005;37(4):333–44.
- [19] Mohebi R, Mehryan SAM, Izadi M, Mahian O. Natural convection of hybrid nanofluids inside a partitioned porous cavity for application in solar power plants. J Therm Anal Calorim 2019;137(5):1719–33.
- [20] Izadi M. Effects of porous material on transient natural convection heat transfer of nano-fluids inside a triangular chamber. Chin J Chem Eng 2020;28(5):1203–13.
- [21] Gustavsen A, Arasteh D, Kohler C, Curcija D. Two-dimensional conduction and cfd simulations of heat transfer in horizontal window frame cavities. ASHRAE Trans 2005;111(1):587–98.
- [22] Gustavsen A, Griffith BT, Arasteh D. Three-dimensional conjugate cfd simulations of internal window frame cavities validated using ir thermography. ASHRAE Trans 2001;107(Pt 2):538–49.
- [23] Lechowska AA, Schnotale JA, Baldinelli G. Window frame thermal transmittance improvements without frame geometry variations: an experimentally validated cfd analysis. Energy Build 2017;145:188–99.

- [24] Xu S, Ganapathysubramanian B. Computational investigation of the impact of glass flexure on thermal efficiency of double-pane windows. J Therm Anal Calorim 2020.
- [25] Santamouris M, Allard F. Natural ventilation in buildings: a design handbook. Farthscan 1998.
- [26] Markatos NC, Pericleous KA. Laminar and turbulent natural convection in an enclosed cavity. Int J Heat Mass Transfer 1984;27(5):755–72.
- [27] Henkes RAWM, Van Der Vlugt FF, Hoogendoorn CJ. Natural-convection flow in a square cavity calculated with low-reynolds-number turbulence models. Int J Heat Mass Transfer 1991;34(2):377–88.
- [28] Barakos G, Mitsoulis E, Assimacopoulos D. Natural convection flow in a square cavity revisited: laminar and turbulent models with wall functions. Int J Numer Methods Fluids 1994;18(7):695–719.
- [29] Lankhorst AM, Hoogendoorn CJ. Numerical computation of high rayleigh number natural convection and prediction of hot radiator induced room air motion. Appl Sci Res 1990;47(4):301–22.
- [30] Hsieh KJ, Lien FS. Numerical modeling of buoyancy-driven turbulent flows in enclosures. Int J Heat Fluid Flow 2004;25(4):659–70.
- [31] Tieszen S, Ooi A, Durbin P, Behnia M. Modeling of natural convection heat transfer. In: Proceedings of the summer program; 1998. p. 287–302.
- [32] Salat J, Xin S, Joubert P, Sergent A, Penot F, Le Quéré P. Experimental and numerical investigation of turbulent natural convection in a large air-filled cavity. Int J Heat Fluid Flow 2004;25(5):824–32.
- [33] Peng S-H, Davidson L. Large eddy simulation for turbulent buoyant flow in a confined cavity. Int J Heat Fluid Flow 2001;22(3):323–31.
- [34] Sergent A, Joubert P, Le Quéré P. Development of a local subgrid diffusivity model for large-eddy simulation of buoyancy-driven flows: application to a square differentially heated cavity. Numer Heat Transfer A Appl 2003;44(8):789–810.
- [35] Van Treeck C, Rank E, Krafczyk M, Tölke J, Nachtwey B. Extension of a hybrid thermal lbe scheme for large-eddy simulations of turbulent convective flows. Comput Fluids 2006;35(8):863–71.
- [36] Zhai Z. Application of computational fluid dynamics in building design: aspects and trends. Indoor Built Environ 2006;15(4):305–13.
- [37] Li Y, Nielsen PV. Cfd and ventilation research. Indoor Air 2011;21(6):442-53.
- [38] Etheridge D. A perspective on fifty years of natural ventilation research. Build Environ 2015;91:51–60.
- [39] Xu S, Gao B, Hsu M-C, Ganapathysubramanian B. A residual-based variational multiscale method with weak imposition of boundary conditions for buoyancydriven flows. Comput Methods Appl Mech Eng 2019;352:345–68.
- [40] Hughes TJR, Mazzei L, Jansen KE. Large eddy simulation and the variational multiscale method. Comput Visualiz. Sci. 2000;3:47–59.
- [41] Hughes TJR, Mazzei L, Oberai AA, Wray A. The multiscale formulation of large eddy simulation: decay of homogeneous isotropic turbulence. Phys Fluids 2001;13: 505–12.
- [42] Bazilevs Y, Calo VM, Cottrell JA, Hughes TJR, Reali A, Scovazzi G. Variational multiscale residual-based turbulence modeling for large eddy simulation of incompressible flows. Comput Methods Appl Mech Eng 2007;197(1):173–201.
- [43] Blocken B. LES over RANS in building simulation for outdoor and indoor applications: a foregone conclusion? Build Simul 2018;11(5):821–70.
- [44] Bazilevs Y, Hughes TJR. Weak imposition of Dirichlet boundary conditions in fluid mechanics. Comput Fluids 2007;36:12–26.
- [45] Xu F, Schillinger D, Kamensky D, Varduhn V, Wang C, Hsu M-C. The tetrahedral finite cell method for fluids: immersogeometric analysis of turbulent flow around complex geometries. Comput Fluids 2016;141:135–54.
- [46] Xu F, Moutsanidis G, Kamensky D, Hsu M-C, Murugan M, Ghoshal A, Bazilevs Y. Compressible flows on moving domains: stabilized methods, weakly enforced

- essential boundary conditions, sliding interfaces, and application to gas-turbine modeling. Comput Fluids 2017;158:201–20.
- [47] Xu F, Bazilevs Y, Hsu M-C. Immersogeometric analysis of compressible flows with application to aerodynamic simulation of rotorcraft. Math Models Methods Appl Sci 2019;29:905–38.
- [48] Xu S, Xu F, Kommajosula A, Hsu M-C, Ganapathysubramanian B. Immersogeometric analysis of moving objects in incompressible flows. Comput Fluids 2019;189:24–33.
- [49] Zhu Q, Xu F, Xu S, Hsu M-C, Yan J. An immersogeometric formulation for freesurface flows with application to marine engineering problems. Comput Methods Appl Mech Eng 2020;361:112748.
- [50] Yan J, Deng X, Xu F, Xu S, Zhu Q. Numerical simulations of two back-to-back horizontal axis tidal stream turbines in free-surface flows. J Appl Mech 2020;87(6).
- [51] Jeanblanc E, He S, Passe U. Occupant-centered building operation strategies for balancing thermal comfort and energy efficiency in warm and humid climates. In: Proceedings of the 9th Windsor Conference: Making Comfort Relevant, NCEUB, Windsor, UK; 2016. p. 7–10.
- [52] ANSI/ASHRAE. Standard 55-2017: thermal environmental conditions for human occupancy. American Society of Heating, Refrigerating and Air-conditioning Engineers, Atlanta, USA; 2017.
- [53] Brooks AN, Hughes TJR. Streamline upwind/Petrov-Galerkin formulations for convection dominated flows with particular emphasis on the incompressible Navier-Stokes equations. Comput Methods Appl Mech Eng 1982;32:199–259.
- [54] Tezduyar TE, Mittal S, Ray SE, Shih R. Incompressible flow computations with stabilized bilinear and linear equal-order-interpolation velocity-pressure elements. Comput Methods Appl Mech Eng 1992;95(2):221–42.
- [55] Johnson C. Numerical solution of partial differential equations by the finite element method. Sweden: Cambridge University Press; 1987.
- [56] Brenner SC, Scott LR. The mathematical theory of finite element methods. 2nd ed. Berlin: Springer; 2002.
- [57] Nitsche J. Über ein Variationsprinzip zur Lösung von Dirichlet-Problemen bei Verwendung von Teilräumen, die keinen Randbedingungen unterworfen sind. Abhandlungen aus dem Mathematischen Seminar der Universität Hamburg 1971; 36:9–15.
- [58] Chung J, Hulbert GM. A time integration algorithm for structural dynamics with improved numerical dissipation: the generalized-α method. J Appl Mech 1993;60: 371–5.
- [59] Jansen KE, Whiting CH, Hulbert GM. A generalized- α method for integrating the filtered Navier-Stokes equations with a stabilized finite element method. Comput Methods Appl Mech Eng 2000;190:305–19.
- [60] Saad Y, Schultz MH. Gmres: a generalized minimal residual algorithm for solving nonsymmetric linear systems. SIAM J Sci Stat Comput 1986;7(3):856–69.
- [61] Shakib F, Hughes TJR, Johan Z. A multi-element group preconditioned GMRES algorithm for nonsymmetric systems arising in finite element analysis. Comput Methods Appl Mech Eng 1989;75:415–56.
- [62] ASHRAE. ASHRAE handbook: fundamentals. American Society of Heating, Refrigerating and Air-conditioning Engineers, Atlanta, USA; 2009.
- [63] Fanger PO. Thermal comfort: analysis and applications in environmental engineering. Copenhagen, Denmark: Danish Technical Press; 1970.
- [64] Fusegi T, Hyun JM, Kuwahara K, Farouk B. A numerical study of three-dimensional natural convection in a differentially heated cubical enclosure. Int J Heat Mass Transfer 1991:34(6):1543–57.
- [65] Mallinson GD, De Vahl Davis G. Three-dimensional natural convection in a box: a numerical study. J Fluid Mech 83(1): 1977; 1–31.
- [66] Krane RJ, Jessee J. Some detailed field measurements for a natural convection flow in a vertical square enclosure. Proceedings of the first ASME-JSME thermal engineering joint conference 1983;1:323–9.